Geoscience Frontiers 8 (2017) 1073–1087

HOSTED BY

Contents lists available at ScienceDirect

China University of Geosciences (Beijing)

Geoscience Frontiers

journal homepage: www.elsevier.com/locate/gsf

Research paper

The Pushtashan juvenile suprasubduction zone assemblage of Kurdistan (northeastern Iraq): A Cretaceous (Cenomanian) Neo-Tethys missing link

Sabah A. Ismail [a], Sarmad A. Ali [a,b], Allen P. Nutman [b,*], Vickie C. Bennett [c], Brain G. Jones [b]

[a] Department of Applied Geology, College of Sciences, Kirkuk University, Kirkuk, 36001, Iraq
[b] GeoQuEST Research Centre, School of Earth & Environmental Sciences, University of Wollongong, Wollongong, NSW 2522, Australia
[c] Research School of Earth Sciences, Australian National University, ACT 0200, Australia

ARTICLE INFO

Article history:
Received 22 July 2016
Received in revised form
27 October 2016
Accepted 1 November 2016
Available online 16 November 2016
Handling Editor: M. Santosh

Keywords:
Pushtashan suprasubduction assemblage
Cretaceous
Zircon U-Pb dating
Hf isotopes
Kurdistan region Iraq
Neo-Tethys

ABSTRACT

The Pushtashan suprasubduction zone assemblage of volcanic rocks, gabbros, norites and peridotites occurs in the Zagros suture zone, Kurdistan region, northeastern Iraq. Volcanic rocks are dominant in the assemblage and consist mainly of basalt and basaltic andesite flows with interlayered red shale and limestone horizons. Earlier lavas tend to be MORB-like, whereas later lavas display island arc tholeiite to boninitic geochemical characteristics. Tholeiitic gabbros intrude the norites and display fractionation trends typical of crystallisation under low-pressure conditions, whereas the norites display calc-alkaline traits, suggesting their source included mantle metasomatised by fluids released from subducted oceanic crust. Enrichment of Rb, Ba, Sr, Th and the presence of negative Nb anomalies indicate generation in a suprasubduction zone setting. Trondhjemite and granodiorite intrusions are present in the volcanic rocks, gabbros and norites. SHRIMP U-Pb dating of magmatic zircons from a granodiorite yields a mean $^{206}Pb/^{238}U$ age of 96.0 ± 2.0 Ma (Cenomanian). The initial ε_{Hf} value for the zircons show a narrow range from +12.8 to +15.6, with a weighted mean of +13.90 ± 0.96. This initial value is within error of model depleted mantle at 96 Ma or slightly below that, in the field of arc rocks with minimal contamination by older continental crust. The compositional bimodality of the Pushtashan suprasubduction sequence suggests seafloor spreading during the initiation of subduction, with a lava stratigraphy from early-erupted MORB transitioning into calc-alkaline lavas and finally by 96 Ma intrusion of granodioritic and trondhjemitic bodies with juvenile crustal isotopic signatures. The results confirm another Cretaceous arc remnant preserved as an allochthon within the Iraqi segment of the Cenozoic Zagros suture zone. Implications for the closure of Neo-Tethys are discussed.

1. Introduction

Ophiolites and allochthonous suprasubduction assemblages are key elements in determining the complicated geological process by which oceans are consumed leading to collisional orogeny. However in many cases, the original tectonic setting of these assemblages is uncertain because they are preserved as disconnected allochthons in a younger orogen. The closure of the Neo-Tethys Ocean is a classic example of such problems. Thus within the Zagros orogenic belt of northeastern Iraq (Kurdistan) the Mesozoic ophiolites and suprasubduction zone complexes are part of a 2000 km-long belt that extends from Troodos Cyprus to Semail Oman (Fig. 1). Due to continuing conflict in the Kurdistan region, there has been very little recent geological research, with particularly sparse geochronological and isotopic data on these suprasubduction zone assemblages. This sparseness of information makes it hard to link them with the more understood geodynamic scenarios in the better documented adjacent regions (i.e., eastern Turkey, southwestern Iran and northern Oman).

Reconstruction of the Iraqi ophiolites and supra-subduction complexes along the Zagros Orogenic Belt is further complicated because they were emplaced during two major episodes; in the Mesozoic and Cenozoic (Ismail et al., 2014), followed by out-of-

* Corresponding author.
E-mail address: anutman@uow.edu.au (A.P. Nutman).
Peer-review under responsibility of China University of Geosciences (Beijing).

http://dx.doi.org/10.1016/j.gsf.2016.11.002

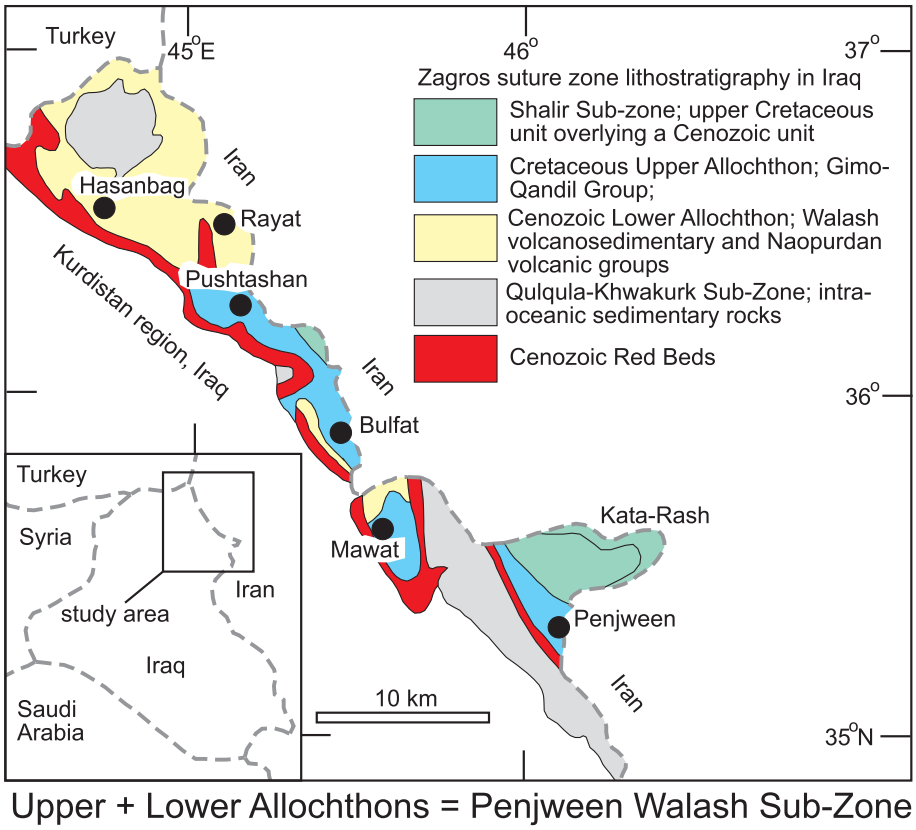

Figure 1. Regional tectonic map of the Kurdistan region in NE Iraq, showing distribution of ophiolites along Zagros Suture Zone. Major tectonic subdivisions after Aswad et al., 2014.

sequence thrusting during final closure in the Neogene (e.g., Shafaii Moghadam et al., 2014). The Mawat, Penjwen, Bulfat, Hasanbag and Shalir assemblages have been identified as Mesozoic in age (Fig. 1; Ali et al., 2012, 2016). Cenozoic ophiolites and suprasubduction assemblages are relatively smaller, less well preserved, and occur as mélange-like disrupted and incomplete fragments within the Eocene Walash-Naopurdan Group. These mélange-type assemblages are typified by the Rayat and Qalander complexes (Arai et al., 2006; Ismail et al., 2009, 2010, 2014).

The Pushtashan assemblage forms part of the Qandil Mountain, Iraqi Kurdistan region, some 130 km north of Sulaymania city (Fig. 2) and consists of volcanic, gabbroic, noritic and rare trondhjemitic-granodioritic components. Only a few internal reports have referred to the Pushtashan complex, as part of reconnaissance studies carried out by the Iraqi Geological Survey during the 1950s and 1960s. For the Pushtashan assemblage we present the first detailed field and petrographic descriptions, whole rock and mineral geochemistry and zircon U-Pb dating by SHRIMP and Hf isotopic data acquired by LA-ICP-MS in order to establish the age and geodynamic setting of these rocks. The Pushtashan assemblage is identified as a Cretaceous (Cenomanian) suprasubduction zone assemblage dominated by mafic rocks, with lesser amounts of felsic intrusive rocks. With its Cretaceous age, it is integrated as another missing link in the Mesozoic history of closure of the middle eastern sector of Neo-Tethys.

2. Geological background

2.1. European–middle eastern remnants of Neo-Tethys

The scattered Mediterranean and middle eastern ophiolites represent a complex orogenic zone formed during progressive Mesozoic to ongoing recent collision of Afro-Arabian and Eurasian continental crust. The Mesozoic ophiolites crop out in four belts; the Jurassic Alpine–Apennine belt of the western Mediterranean, the Jurassic Dinaride–Hevenide complex of the western Balkan peninsula, the Jurassic–Cretaceous bodies of eastern Greece and central Turkey and late Cretaceous complexes of southern Turkey, Cyprus, northern Syria and extending through Zagros Mountains (Iraq-Iran) to Oman (Dilek and Moores, 1990; Lagabrielle and Cannat, 1990; Smith, 1993; Dilek et al., 2007; Dilek and Thy, 2009). The late Cretaceous ophiolites include the Pre-Arabian ophiolites along the Bitlis-Zagros suture zone and represent remnants of the southern Neo-Tethyian oceanic lithosphere that in the latest Cretaceous were obducted by a series of collisions of intra-oceanic arc-trench systems with continental margins (Dilek et al., 1999).

2.2. Geology of the Zagros suture zone

The Iraq Zagros Suture Zone (Fig. 1) forms part of the larger Zagros Belt which runs ~2000 km, extending from the Balkan Peninsula through the Anatolian Taurus mountains to the Iranian Zagros mountains, and marks the boundary of the Arabian and the Iranian continents in northeastern Iraq. Within the Iraq Zagros Suture, there are two allochthonous units (lower and upper) that formed within Neo-Tethys (Jassim and Goff, 2006). The units were obducted over the Arabian Plate during two distinct late Cretaceous and Neogene phases of obduction and collision (Fig. 3; Jassim and Goff, 2006). Three tectonic zones are identified within Iraq sector of the Zagros Suture Zone. The Qulqula-Khwakurk Zone forms units from the southern side of Neo-Tethys that were obducted and sutured to the Arabian plate and then folded during the late Cretaceous. The Penjween-Walash zone is a Neotethys unit that consists

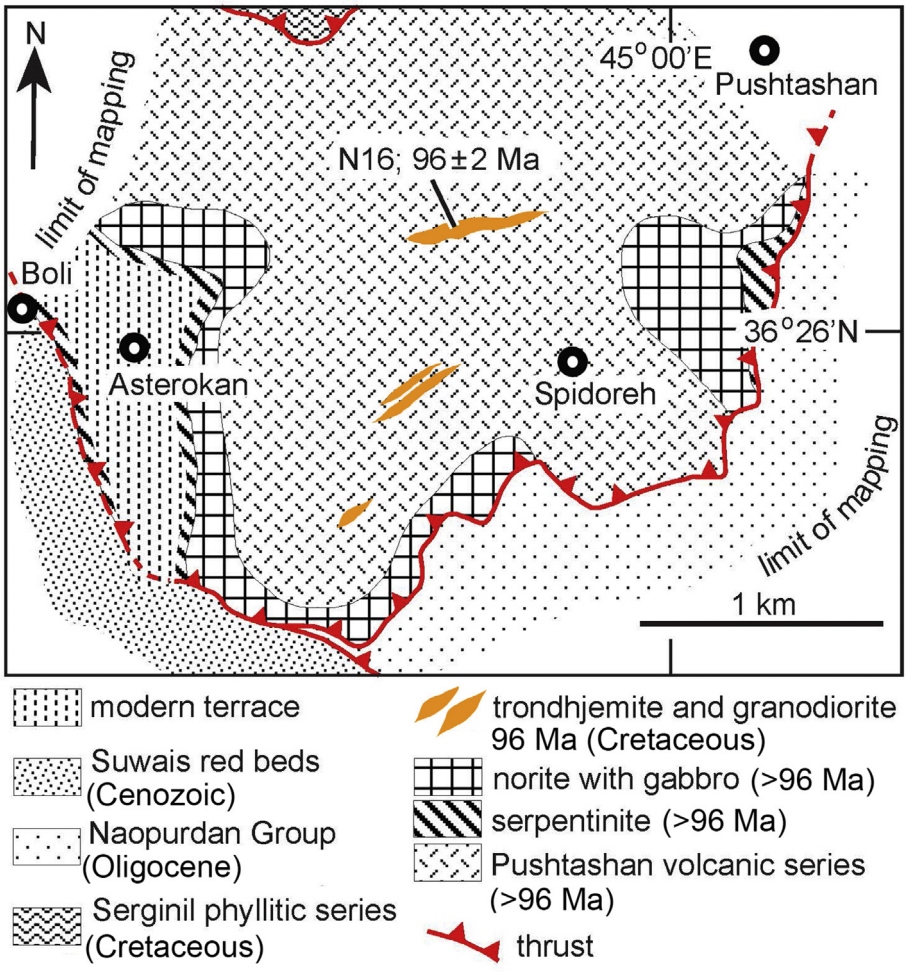

Figure 2. Geologic map of Pushtashan ophiolite (modified from Bolton, 1956).

of three thrust sheets: lower Naopurdan, the middle Walash and the upper Qandil units. The first two thrust sheets form the Cenozoic ophiolites and suprasubduction complexes. The Qandil sheet contains Cretaceous ophiolites and suprasubduction zone complexes that include the Bulfat, Mawat, Penjween and Pushtashan occurrences (Ismail et al., 2014). These complexes were obducted over the Qulqula–Khwakurk Zone.

2.3. Geological background of the Pushtashan area

The geological setting of the Pushtashan area is based on recent field work by the first two authors integrated with observations in survey reports by Bolton (1956) and Roulkovsky (1961). The Pushtashan assemblage is zoned in shape (Fig. 2). Volcanic rocks occur in the upper part of the allochthon, intruded by plutonic rocks. The plutonic complexes are composed largely of gabbro and norite, with associated felsic veins and serpentinised peridotites. The gabbros and norites form a sill intruded into the volcanic rocks (Buday and Jassim, 1987). The maximum width of the rock assemblage is 6 km. It is best exposed along the edge of the thrust front for a distance of 16 km in the Pushtashan valley (Bolton, 1956). There is a major thrust between the Pushtashan assemblage and the underlying Oligocene Naopurdan Group of grey flysch of the Razga series (Ali et al., 2013; Fig. 2). The Pushtashan assemblage consists of three units. Uppermost are volcanic rocks, with a maximum preserved thickness of approximately 1000 m, consisting of vesicular pillow basalt and andesite with red calcareous mudstones (Fig. 4a). Quartz veins found amongst basalts and andesites show some copper mineralisation. There is a major structural break (thrust fault) between the volcanic rocks and the overlying Cretaceous Qandil Group (Fig. 2; the Sirginil phyllite series of Bolton, 1956). The Pushtashan plutonic rocks that intrude the volcanic rocks are approximately 140 m thick and form the middle part of the Pushtashan assemblage. They consist mainly of norite (Fig. 4b) with irregular small lenses of gabbro and hornblendite (0.2–0.5 m). Pegmatitic gabbro veins (0.5 m thick) are common, and extend for up to 100 m, generally parallel to the floor of the norite body (Roulkovsky, 1961). Granitoid intrusions (mostly trondhjemite) 5 to 40 m thick are present in the upper part of the norite body and the volcanic rocks. The ultramafic rocks form about 10% of the complex and occur in its lower part (Fig. 4c). The ultramafic rocks (maximum thickness 40 m) consist of serpentinised peridotites locally altered to chrysotile asbestos and magnesite.

3. Analytical methods

3.1. SHRIMP U-Pb analytical method and data appraisal

Zircons were concentrated using heavy liquid and isodynamic separation techniques at the mineral separation laboratory of the Research School of Earth Sciences, the Australian National University (ANU). Using a binocular microscope, the concentrate was

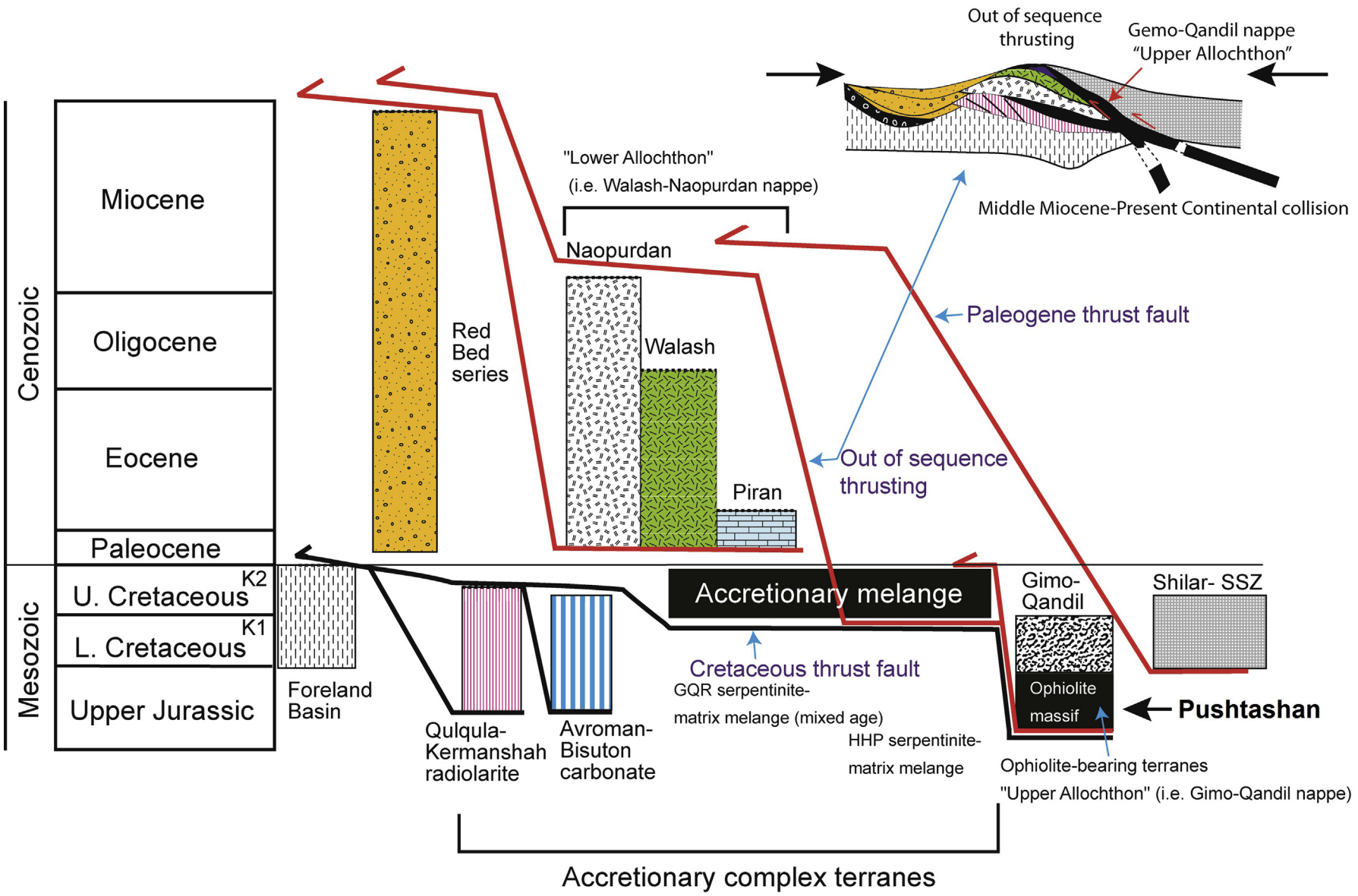

Figure 3. Summary of the tectono-stratigraphic relationships in the Kurdistan section of the Zagros suture zone (Figure after Ali et al., 2014).

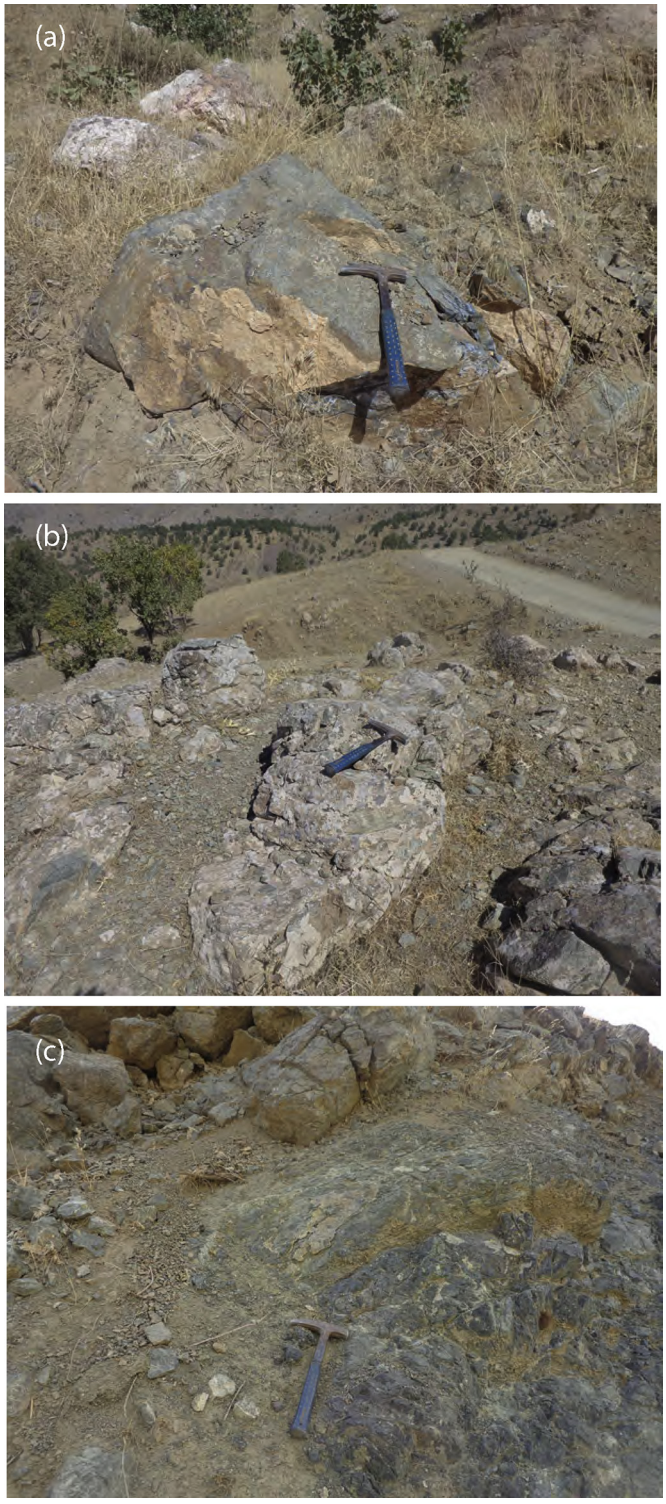

Figure 4. Field photographs for Pushtashan ophiolite: (a) Volcanic rocks with sedimentary interlayers. (b) Norite intrusion. (c) Serpentinite in the base of the assemblage.

hand-picked and along with reference Temora zircons (Black et al., 2003), the selected grains were cast in an epoxy resin disc. This was ground to a mid-section level through the grains and then polished. Cathodoluminescence (CL) imaging was used to document the grains.

U-Th-Pb analyses of the zircons were undertaken on the ANU SHRIMP 2 instrument following analytical protocols of Williams (1998), with the raw data being reduced using ANU software 'PRAWN' and 'Lead'. Measurements of $^{206}Pb/^{238}U$ in unknown zircons were calibrated using the Temora standard (U-Pb ages concordant at 417 Ma; Black et al., 2003). The reference zircon SL13 (U = 238 ppm) located in a set-up mount was used to calibrate U and Th abundance in the unknown zircons. The populations consist of magmatic zircons with near concordant ages that are all within analytical error with each other, i.e. without dispersion in $^{206}Pb/^{238}U$. Therefore, the ^{207}Pb correction method (Compston et al., 1984) was used to correct for (minor) common Pb, with the Zartman (1981) orogene model Pb composition for the likely age of the zircons. The ISOPLOT program (Ludwig, 2003) was used to assess and plot the reduced and calibrated data. Regression in $^{207}Pb/^{206}Pb - ^{238}U/^{206}Pb$ space (prior to correction for common Pb) and $^{206}Pb/^{238}U$ ratios (common Pb corrected) were used to calculate the U-Pb ages. In the former, the lower intercept with concordia is interpreted as the radiogenic (i.e. magmatic) dominant component, whereas the intercept with the $^{207}Pb/^{206}Pb$ axis (i.e., when $^{238}U/^{206}Pb = 0$) is the $^{207}Pb/^{206}Pb$ of a minor non-radiogenic common Pb component. Calculated ages for the whole population are presented at 95% confidence and are rounded to the nearest hundred thousand years. The results are plotted in a Tera-Wasserburg Concordia diagram prior to correction for common Pb. The reason for plotting them *without* correction for common Pb is to demonstrate that with the small amount of common Pb in these zircons, most of the data already have close to concordant U-Pb ages, prior to correction.

3.2. LA-MC-ICPMS zircon Lu-Hf isotopes

Zircon Lu-Hf isotopic compositions were determined from the same zircons used for U-Pb SHRIMP analyses, during a single analytical session using the RSES ThermoFinnigan Neptune multi-collector ICPMS coupled to a Lambda Physik ArF, 193 nm excimer laser system with a 'HelEx' sample cell, following methods described by Hiess et al. (2009). Analysis of a gas blank and a suite of 7 reference zircons with a range of $^{176}Hf/^{177}Hf$ and $^{176}Lu/^{177}Hf$ ratios (Monastery, Mud Tank, Plesovice, QGNG, Temora-2, R33 and FC1) were performed systematically after every 10–12 sample spot analyses throughout the session. The details of the analytical method and instrumental set-up are provided in the Supplementary Data.

Initial $^{176}Hf/^{177}Hf$ ratios for each spot were calculated using SHRIMP measured U-Pb ages, present day CHUR compositions of $^{176}Hf/^{177}Hf = 0.282785 \pm 11$, $^{176}Lu/^{177}Hf = 0.0336 \pm 1$ (Bouvier et al., 2008), and a $\lambda^{176}Lu$ decay constant of $1.867 \pm 8 \times 10^{-11}$ y^{-1} (Scherer et al., 2001; Söderlund et al., 2004). Complete Lu-Hf isotopic data for the sample zircons and for zircons for the 7 reference materials are given in Supplementary Data Tables 1 and 2.

3.3. Major element and trace element analyses

Whole-rock major- and trace-element X-ray fluorescence (XRF) analysis was carried out using a Spectro-Analytical Instrument (XEPOS) energy-dispersive spectrometer fitted with a Si-diode detector at the School of Earth and Environmental Sciences, University of Wollongong, Australia, following the methods of Norrish and Chappell (1977). Major elements were measured on samples fused with Li borate, whereas trace elements were analysed from pressed pellets bonded with polyvinyl acetate (PVA). Calibration was made against a wide range of international reference materials and laboratory standards previously calibrated against synthetic standards. Loss-on-ignition was determined by heating a separate aliquot of rock powder at 1000 °C. The samples were analysed at the Australian Laboratory Services (ALS) at Brisbane,

Australia, for their rare earth element (REE) and other trace-element concentrations, using inductively coupled plasma mass spectrometry (ICP-MS).

3.4. Electron microprobe mineral analyses

Microprobe analyses were carried out on polished thin sections utilising a fully automated, Cameca SX100 electron microprobe at Macquarie University, fitted with five wavelength dispersive spectrometers (WDS) and a Princeton Gamma Tech (PGT) energy dispersive system (EDS). The operating conditions were: accelerating voltage 15 kV; beam current 20 nA; beam size focused 1–2 μm; and count times 20 s (10 s peak, 10 s background). The standards used were: Si, Ca—wollastonite; Al—kyanite, Na—albite; Ti—rutile; Cr—Cr metal; Fe—hematite; Mn—spessartine; Mg—forsterite; K—orthoclase; and Ni—Ni metal. The purpose of these analyses was to establish the magmatic feldspar and pyroxene compositions in these variably-altered rocks.

4. Petrography and mineral chemistry

Petrographic studies were undertaken on 29 thin sections from volcanic and intrusive mafic rocks and granitoids. The primary igneous minerals in all samples are generally partly altered to chlorite, secondary amphibole, calcite, fine-grained clay minerals, sericite, zeolites, and secondary albite. Basalts are dark green, and contain small phenocrysts of plagioclase and clinopyroxene in glassy groundmass (Fig. 5a). Andesites are porphyritic with some amygdules filled with chlorite (Fig. 5b). Plagioclase grains are idiomorphic to subidiomorphic. Clinopyroxenes are generally subhedral to euhedral, and variably altered to chlorite and

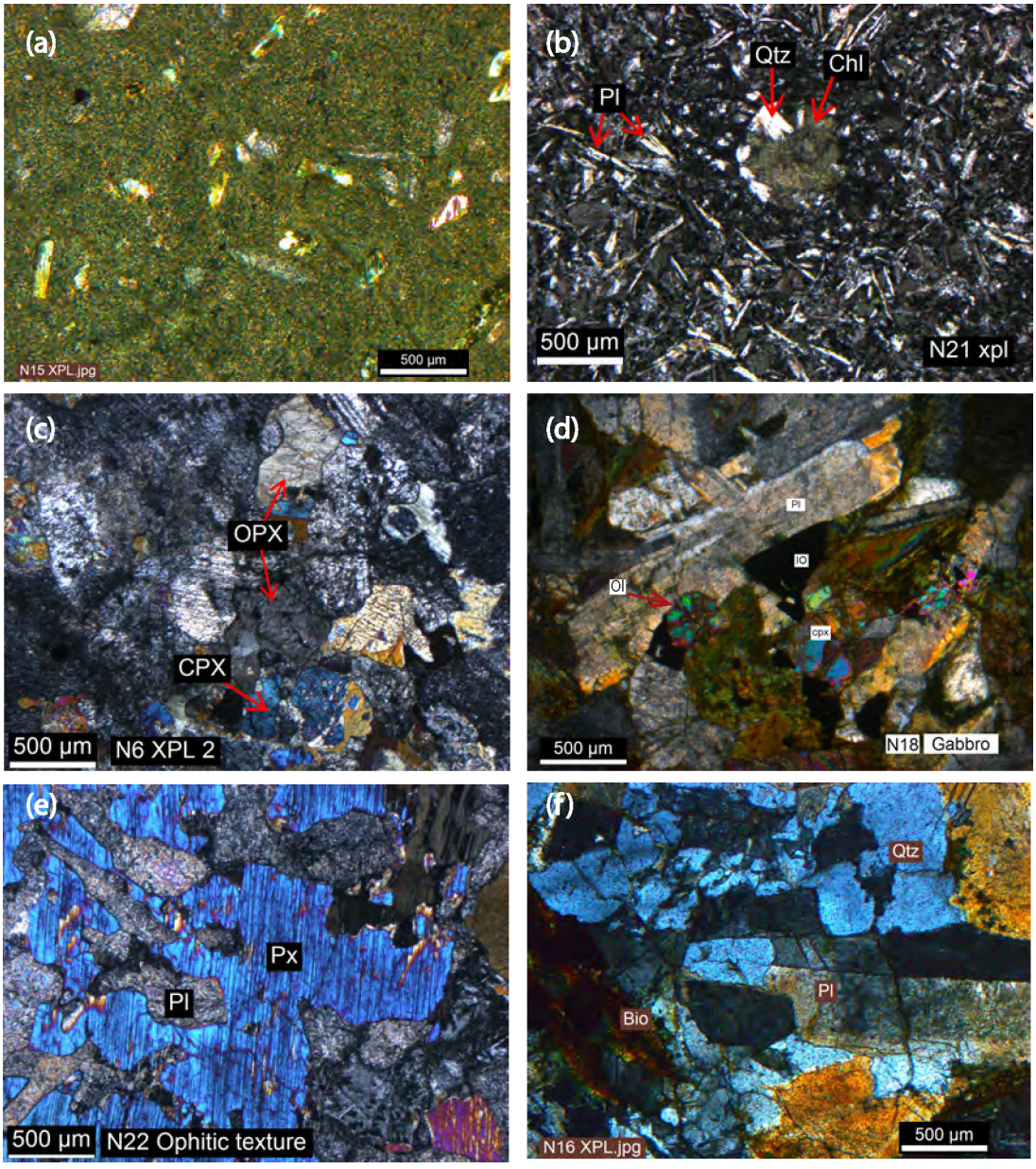

Figure 5. Photomicrographs of Pushtashan ophiolite rocks: (a) basalt with porphyritic texture; (b) amygdaloidal texture with amygdules filled by chlorite; (c) norite with relict igneous clinopyroxene; (d) olivine-bearing gabbro; (e) norite with ophitic texture; (f) trondhjemite N16.

secondary amphibole. Anorthoclase occurs in the groundmass as microlites. Mineral analyses are presented in Table 1.

The norite body is generally fine to medium grained with patchy occurrence of pegmatitic norite. They contain calcic plagioclase (An_{70-93}, Table 1), orthopyroxene (ferroan enstatite – En_{68-75}), hornblende, and subordinate clinopyroxene (Fig. 5c). The hornblende mostly overgrows pyroxenes. Some anhedral bastite pseudomorphs after pyroxene are present. Patchy occurrence of pegmatitic norite is recognised in these rocks and they carry orthopyroxene crystals up to 3 cm across between large tabular plagioclase grains.

Irregular small lenses of gabbros and pegmatitic gabbro veins extend for hundreds of metres, generally parallel to the floor of the norite body. They are light grey in colour, medium to coarse grained, generally fresh in appearance. These gabbros comprise Na rich plagioclase (An_{35}), hornblende, diopside, relics of orthopyroxene and olivine (Fig. 5d). Ilmenite, rutile, titanite and magnetite are accessory minerals. Most of the gabbro shows typically ophitic to subophitic texture (Fig. 5e), with early-formed plagioclase crystals in mutual contact with each other and later formed olivine and clinopyroxene grains occupying interstitial spaces. This textural observation suggests cumulate origin of the gabbro (cf. Irvine, 1982). Plagioclase, the most common mineral phase, occurs as subhedral tabular grains (0.7 to 6.3 mm in size) with well-developed twin lamellae (Fig. 5d). Olivine (0.5 to 3.7 mm in size) is the next most dominant mineral and is intensively fractured with alteration stains (reddish brown in colour) present along fractures.

The felsic rocks are mainly trondhjemite and granodiorite and form minor 5–40 m thick intrusions (Roulkovsky, 1961). The trondhjemites and granodiorites are medium grained rocks that are light grey colour and have a hypidiomorphic texture (Fig. 5f). Plagioclase with quartz are the essential minerals, with lesser alkali-feldspar, biotite and rare amphibole. Ilmenite, titanite, rutile and magnetite are accessory minerals. A single sample of true granite rock is composed mainly of quartz, alkali feldspar, biotite with accessory titanite, rutile, tourmaline and zircon.

5. Zircon U-Pb-Hf results

5.1. SHRIMP zircon ages and Hf isotopic signatures

Sample N16 (Fig. 2) gave a small yield of mostly <100 μm long prismatic to equant, euhedral, colourless zircons. In CL images the grains display domains of well-preserved igneous oscillatory zoning parallel to the grain margins, but with large amounts of patchy recrystallisation (Fig. 6). Neither inherited cores nor post-magmatic overgrowths are present. In Backscattered Electron (BSE) images (Fig. 6) and in reflected light images the zircons show extensive pitting concentrated in the recrystallisation domains. This style of zircon texture resembles that ascribed to alkaline fluids causing recrystallisation and dissolution in a suprasubduction zone setting (Rubatto et al., 2008). U content ranges from 724 to 267 ppm. The analytical sites with the least disturbed magmatic oscillatory zoning (grains 1 and 2, Fig. 6) have the highest Th/U ratios >1.0, whereas sites encompassing more recrystallisation have lower Th/U (0.97–0.65; Table 2). Nine U-Pb analyses were undertaken on seven zircons, with the focus (3 analyses) on grain #2 with the best-preserved oscillatory zoning. Compositions are dominated by radiogenic Pb giving mostly close to concordant ages, and have U-Pb ages within error of each other (Table 2, Fig. 7). Regression of the data yielded a lower Concordia intercept of 96.0 ± 2.1 (MSWD = 0.42) whereas after correction for common Pb by the ^{207}Pb method, all data yielded a weighted mean $^{206}Pb/^{238}U$ age of 95.0 ± 1.7 Ma (MSWD = 0.64). The weighted mean age of the four sites (grains 1 and 2) with the best-preserved oscillatory-zoned zircon is 96.0 ± 2.0 Ma (MSWD = 0.61) whereas the sites dominated by recrystallization with dissolution domains yielded a statistically indistinguishable age of 93.1 ± 3.5 Ma (MSD = 0.46). This demonstrates that the recrystallisation was late magmatic or occurred shortly after, and that it did not occur during a much younger event. We stress here that these domains consist of non-metamict zircon, which formed by recrystallization of the magmatic zircon in a late-, to immediately post-magmatic event. A key feature indicating recrystallisation rather than metamictisation is the low common Pb content of all analysed domains. Thus 96.0 ± 2.0 Ma age (Cenomanian) is interpreted as the time of igneous crystallisation of sample N16.

Fifteen Lu-Hf isotopic determinations were undertaken on 15 zircons (Table 3). Two of these were undertaken on grains # 2 and 4 of the U-Pb data set, whereas the others (with prefix H) were on a random selection. Analysis H11 ablated through the grain after only a couple of time slices, and yielded anomalous data. It is not considered further in the discussion below. Using the zircon crystallisation age of 96 Ma, the initial ε_{Hf} values show a narrow range, from +12.8 to +15.6 (Table 3), with a weighted mean of 13.90 ± 0.96 (95% confidence, MSWD = 0.96). Thus the data fall

Table 1
Mineral analyses from Pushtashan igneous rocks (oxides in wt.%, trace elements in ppm).

Rock	Basalt		Gabbro				Norite			Granodiorite			
Mineral	plag	pyrox	plag	pyrox	ilm	tit	plag	pyrox	amph	alk-feld	bio	tit	rut
SiO_2	53.3	50.19	59.55	50.75	0.21	30.03	39.73	53.58	48.17	65.16	32.1	26.6	4.07
TiO_2	0.04	0.33	n.d.	0.71	51.8	28.57	n.d.	0.03	0.11	nd	n.d.	31.02	81.72
Al_2O_3	31.01	4.98	25.43	3.27	n.d.	5.35	29.57	0.24	5.12	22.24	21.78	2.66	n.d.
FeO	0.74	16.93	0.3	9.39	43.67	6.72	0.49	6.45	17.25	0.73	18.88	8.67	7.19
MnO	n.d.	0.25	n.d.	0.26	2.68	0.12	0.13	0.3	0.25	nd	0.48	n.d.	n.d.
MgO	0.27	12.95	n.d.	15.75	0.15	2.67	0.14	14.83	11.95	nd	8.33	0.05	n.d.
CaO	9.38	11.89	7.33	19.63	0.08	22.69	21.42	25.2	12.42	0.38	0.43	24.37	3.69
Na_2O	5.61	0.47	7.59	0.33	n.d.	n.d	0.88	n.d.	0.23	11.02	0.19	n.d.	n.d.
K_2O	0.87	0.06	0.1	n.d.	n.d.	n.d.	n.d.	n.d.	0.58	1.35	1.37	n.d.	n.d.
Si	2.36	1.94	2.65	1.87	0.01	1.23	1.68	1.97	7.29	11.44	5.32	1.76	0.06
Ti	0.00	0.01	-	0.02	2.00	0.89	-	0.00	0.01	-	-	0.68	0.87
Al	1.62	0.23	1.33	0.14	-	0.26	1.26	0.01	0.91	4.60	4.25	0.09	-
Fe	0.03	0.55	0.01	0.20	1.87	0.23	0.02	0.20	2.18	0.11	2.62	0.21	0.09
Mn	-	0.01	-	0.01	0.12	0.00	0.01	0.01	0.03	0.00	0.07	-	-
Mg	0.02	0.75	-	0.87	0.01	0.16	0.01	0.81	2.70	0.00	2.06	0.00	-
Ca	0.45	0.49	0.35	0.78	0.00	1.00	0.97	0.99	2.02	0.07	0.08	0.76	0.06
Na	0.48	0.04	0.66	0.02	-	-	0.07	-	0.07	3.75	0.06	-	-
K	0.05	-	0.01	-	-	-	0.00	-	0.11	0.30	0.29	-	-

plag = plagioclase, pyrox = pyroxene, amph = amphibole, alk-feld = alkali feldpsar, bio = biotite, ilm = ilmenite, tit = titanite, rut = rutile.

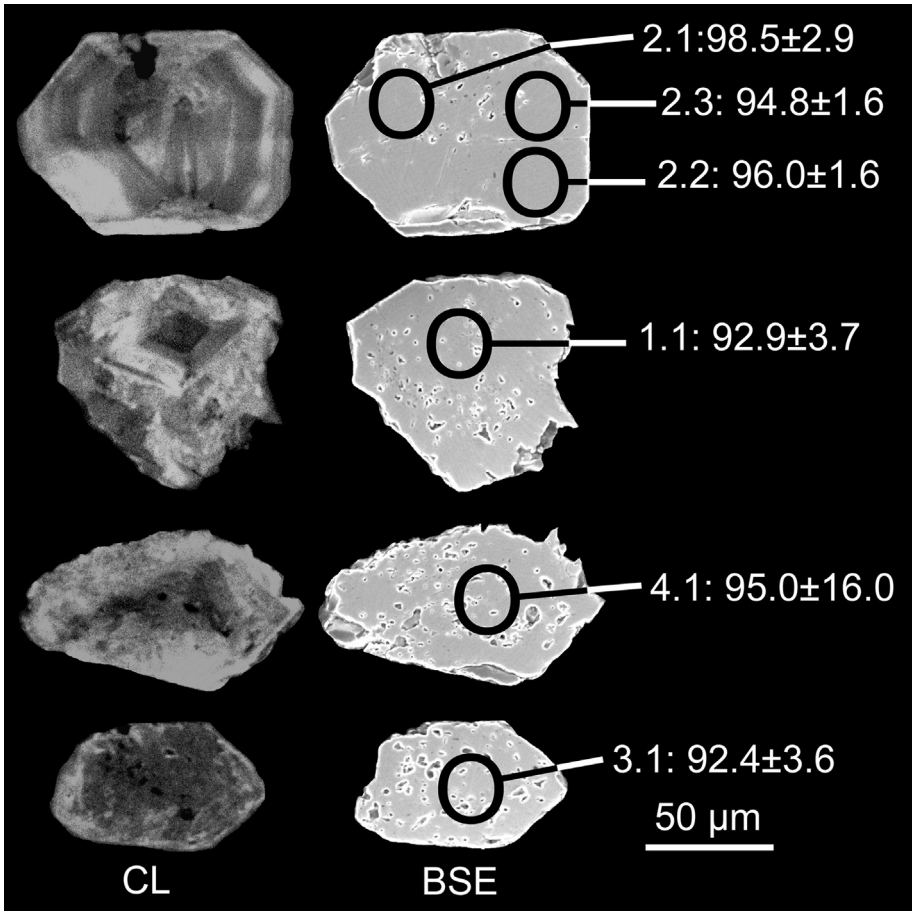

Figure 6. Cathodoluminescence (CL) and backscattered electron (BSE) images of N16 zircons. Grains #1 and #2 are the two with the best preserved oscillatory-zoned igneous zoning. The other grains are representative of the whole population, showing variable degrees of recrystallisation and corrosion to give voids. $^{206}Pb/^{238}U$ ages (Ma) are given with 1σ analytical uncertainties.

within error of model depleted mantle at 96 Ma (DM; with a modern value of +17 to +16), or slightly below that, in the field of arc rocks with minimal contamination by older continental crust (Fig. 8).

6. Whole rock geochemistry

The samples exhibit high loss-on-ignition (LOI) values (2.67–6.14 wt.%; Table 4 and Supplementary Table 2), indicating low-grade metamorphism and/or fluid-assisted alteration processes (Pandarinath et al., 2008). However, despite the alteration, most major elements, the REE and high field strength element concentrations exhibit coherent variation patterns and do not appear to have been greatly disturbed. Therefore, as demonstrated by Polat and Hofmann (2003), these elements preserve information on igneous petrogenesis.

6.1. Volcanic rocks

Three samples of the volcanic rocks show variation in SiO_2 (45.23–52.72 wt.%) and Al_2O_3 (14.08–14.74 wt.%). Variations (wt.%) for other oxides are: CaO 2.15–10.67; MgO 4.49–7.65; $Fe_2O_3{}^t$ (total

Table 2
SHRIMP zircon U-Pb data of trondhjemite sample N16.

Spot	Site	U/ppm	Th/ppm	Th/U	$^{204}Pb/^{206}Pb$	$^{238}U/^{206}Pb$ (meas)	$^{207}Pb/^{206}Pb$ (meas)	Age $^{206}Pb/^{238}U$ (corr)
1.1	m, osc, eq	609	737	1.21	0.0008 ± 0.0004	68.26 ± 4.02	0.0548 ± 0.0021	92.9 ± 3.7
2.1	e, osc, p	696	977	1.40	0.0005 ± 0.0002	64.78 ± 1.68	0.0499 ± 0.0014	98.5 ± 2.9
2.2	e, osc, p	704	906	1.29	0.0003 ± 0.0002	66.61 ± 1.20	0.0482 ± 0.0017	96.0 ± 1.6
2.3	e, osc, p	594	652	1.10	0.0004 ± 0.0004	67.44 ± 1.25	0.0484 ± 0.0015	94.8 ± 1.6
3.1	m, h, p	643	470	0.73	0.0019 ± 0.0004	67.53 ± 3.51	0.0675 ± 0.0024	92.4 ± 3.6
4.1	m, h, p	724	472	0.65	0.0002 ± 0.0001	66.74 ± 2.37	0.0572 ± 0.0014	95.0 ± 16.0
5.1	e, h, p	420	409	0.97	0.0052 ± 0.0012	65.55 ± 2.87	0.1041 ± 0.0071	90.7 ± 3.8
6.1	m, h, p	267	198	0.74	0.0025 ± 0.0010	67.06 ± 2.84	0.0750 ± 0.0045	92.0 ± 3.5
7.1	m, h, p	469	456	0.97	0.0060 ± 0.0011	63.28 ± 2.81	0.0781 ± 0.0053	97.3 ± 3.7

Spot: x.y = grain followed by analysis number.
Site: m = middle, e = end, p = prismatic grain, eq = equant grain, osc = oscillatory zoned, h = homogeneous/etched.
Isotopic ratios and ages: meas = measured, corr = corrected for common Pb (Zartman (1981) 100 Ma model orogene Pb).
Analytical errors: all are reported at 1σ level.

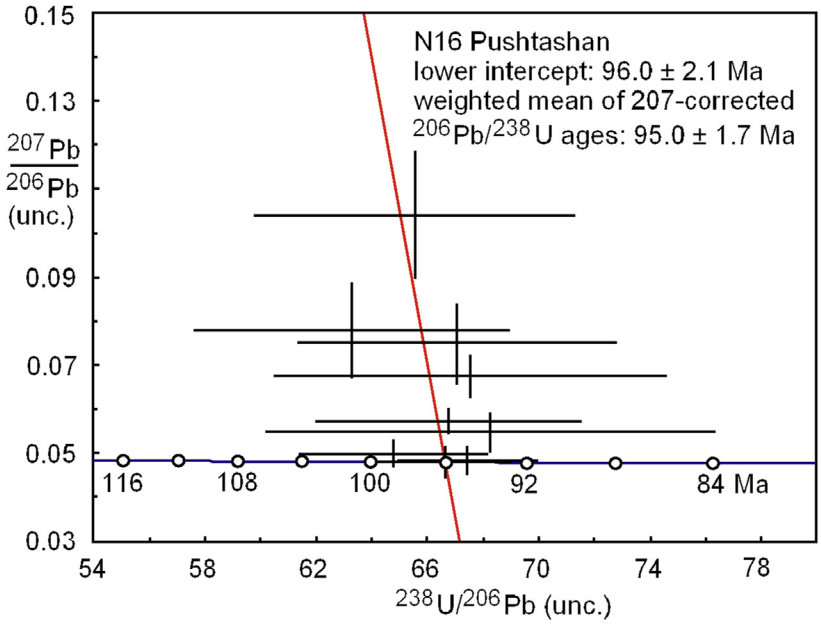

Figure 7. $^{238}U/^{206}Pb - {}^{207}Pb/^{206}Pb$ plot, uncorrected for common Pb. The regression chord gives one method of determining the age of the radiogenic component (lower Concordia intercept). Analytical errors are depicted at the 2σ level.

Table 3
Lu-Hf isotopic data of trondhjemite sample N16.

Grain	$^{176}Lu/^{177}Hf$	Measured[a] $^{176}Hf/^{177}Hf$	$\varepsilon_{Hf}(0)$ In run errors only	U-Pb age (Ma)	Initial $^{176}Hf/^{177}Hf$	$\varepsilon_{Hf}(t)$	T_{DM}[b] (Ga)
2	0.01069 ± 0.00011	0.28316 ± 0.00003	13.2 ± 1.0	96	0.28314	14.65	0.18
4	0.00565 ± 0.00017	0.28310 ± 0.00002	11.0 ± 0.7	96	0.28309	12.79	0.25
H1	0.00869 ± 0.00012	0.28311 ± 0.00003	11.4 ± 1.0	96	0.28309	12.97	0.26
H2	0.00774 ± 0.00041	0.28311 ± 0.00003	11.3 ± 1.1	96	0.28309	12.97	0.25
H3	0.00287 ± 0.00006	0.28315 ± 0.00001	12.9 ± 0.5	96	0.28315	14.88	0.15
H4	0.00464 ± 0.00007	0.28315 ± 0.00002	13.1 ± 0.8	96	0.28315	14.89	0.15
H5	0.01119 ± 0.00044	0.28314 ± 0.00003	12.7 ± 1.0	96	0.28312	14.09	0.21
H6	0.00881 ± 0.00013	0.28315 ± 0.00004	13.0 ± 1.5	96	0.28314	14.54	0.18
H7	0.00499 ± 0.00009	0.28315 ± 0.00003	12.9 ± 1.0	96	0.28314	14.69	0.16
H8	0.00827 ± 0.00054	0.28303 ± 0.00004	8.8 ± 1.4	96	0.28302	10.44	0.38
H9	0.00308 ± 0.00007	0.28314 ± 0.00002	12.6 ± 0.6	96	0.28314	14.55	0.16
H10	0.00845 ± 0.00038	0.28310 ± 0.00003	11.1 ± 0.9	96	0.28308	12.72	0.27
H11*	0.00193 ± 0.00006	0.28199 ± 0.00002	−27.9 ± 0.6	96	0.28199	−25.94	1.81
H12	0.00418 ± 0.00004	0.28317 ± 0.00004	13.7 ± 1.3	96	0.28317	15.62	0.12
H13	0.00734 ± 0.00005	0.28313 ± 0.00002	12.0 ± 0.7	96	0.28311	13.70	0.22

H11* ablated through in a few time slices, poor unstable data, not used in assessment.
Uncertainties, except where noted, are quoted at 1σ.
[a] Uncertainty in initial ratios are 2σ and include the 2σ uncertainty in the Plesovice standards (Supplementary Table 2) added in quadrature.
[b] Depleted mantle (DM) model ages calculated using values for DM of $^{176}Hf/^{177}Hf = 0.2832$ and $^{176}Lu/^{177}Hf = 0.0393$ (Iizuka et al., 2010).

iron) 12.21–16.27; TiO_2 1.01–3.35; P_2O_5 0.09–0.51; and MnO 0.12–0.21 (Table 4 and Supplementary Data Table 2). Na_2O and K_2O values range from 2.58 to 5.08 wt.% and 0.08–3.05 wt.%, respectively. Using the Nb/Y versus Zr/TiO_2 plot of Winchester and Floyd (1977) the mafic rocks fall in the sub-alkaline basalt to andesite/basalt field, and the single analysis of a felsic intrusion falls in the rhyodacite/dacite field (Fig. 9). Most major oxides display a clear negative or positive correlation with increasing MgO content, reflecting the dominant role of igneous fractional crystallization processes preserved in the samples. In the AFM triangle, all the Pushtashan basalt samples fall in the tholeiitic field of Irvine and Baragar (1971; Fig. 10a). The volcanic samples plot in the IAT and MORB field on the TiO_2-MnO-P_2O_5 diagram of Mullen (1983; Fig. 10b).

Compatible trace elements (Cr, Co, Ni, and V) show significant positive correlation with MgO, again indicative of a preserved igneous fractionation trend. However, the large ion lithophile elements scatter with respect to MgO, whereas the incompatible high field strength elements (HFSEs) such as Zr, Y, Th, Nb, Ta, and Ce show clearer negative correlation trends with MgO. The chondrite-normalised REE patterns for the volcanic samples are flat and around 10 times of chondrite values (normalising values from Sun and McDonough, 1989) with slightly negative Eu anomalies, indicative of plagioclase fractionation (Fig. 11b).

6.2. Plutonic mafic rocks

The mafic rocks have less than 50 wt.% SiO_2 (Table 4 and Supplementary Data Table 2). Most major oxides display a clear negative or positive correlation within increasing MgO content, reflecting that fractional crystallisation processes have been preserved in their chemistry. Major element contents show that the

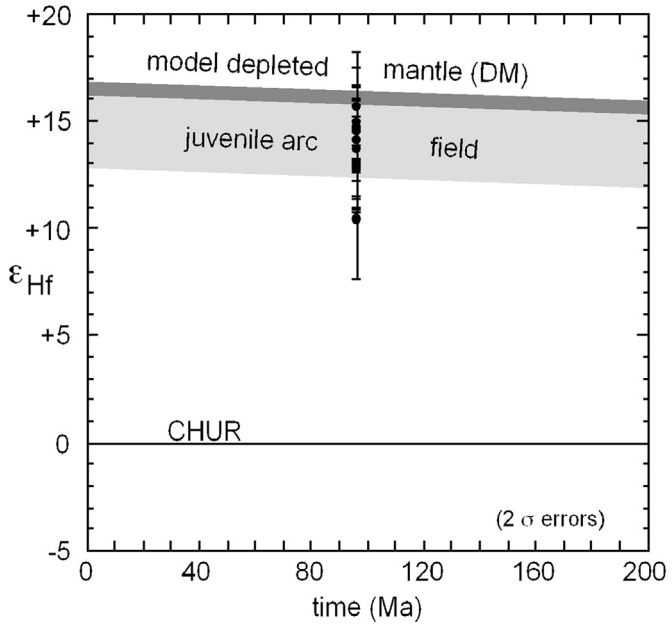

Figure 8. Time (Ma) – ε_{Hf} plot for N16 zircons, showing the initial values at 96 Ma (the U-Pb age of magmatic zircon).

norites and gabbros do not belong to the same line of descent, because for a given MgO content, norites are richer in Al_2O_3, MgO, CaO and poorer in SiO_2, TiO_2, Fe_2O_3, K_2O and Na_2O compared with the gabbros. The norite samples have a high MgO content (>11 wt.%) and Mg# (80), pointing to a cumulate character. The norites define a typical calc-alkaline trend on the SiO_2 vs. FeO^t/MgO diagram of Miyashiro (1974). The gabbros have lower MgO content (<7 wt.%) and Mg# (54). Gabbros mostly plot in the tholeiitic compositional trend on the SiO_2 vs. FeO^t/MgO diagram of Miyashiro (1974). Trace elements that are compatible in clinopyroxene, such as V, decrease rapidly with MgO, and behave similarly to TiO_2 contents in these rocks (Table 3 and Supplementary Data Table 2). Ni and Cr are more abundant in the norites than in the gabbros.

Normalised to chondrite values of Sun and McDonough (1989), the norites have flat middle to heavy REE patterns with slight depletion of the light REE, and positive Eu anomalies that are related to plagioclase accumulation (Fig. 11a). The gabbros are generally more enriched in REE content (10 times chondrite) with also flat middle to heavy REE patterns with slight depletion of the light REE, but without Eu anomalies (Fig. 11b). In multi-element spider plots normalised to primitive mantle of Sun and McDonough (1989), the norites show negative anomalies in high field strength elements (Th, Nb, Zr, and Ti) whereas for the gabbros no such anomalies are observed (Fig. 11c,d).

6.3. Felsic intrusive rocks

Major, trace, and REE data of the Pushtashan complex trondhjemite N16 used for zircon U-Pb-Hf studies is presented in Table 4. The well-preserved igneous texture and the relatively low loss on ignition (LOI) of the sample suggest that effects of post-emplacement alteration are minor, with the analysis largely reflecting the primary composition of the rock. The sample is peraluminous and plots within the trondhjemite field of the Barker (1979) granitoid classification diagram. It has high SiO_2 (74.98 wt.%), high Na_2O (5.24 wt.%), and is low in K_2O (0.31 wt.%). The chondrite-normalised REE pattern of N16 (Fig. 11b) is only slightly fractionated ($(La/Yb)_N$ = 0.94), is enriched approximately 20 times chondrite and shows a small negative Eu anomaly.

7. Discussion

7.1. Age and isotopic signature of the Pushtashan assemblage

Magmatic zircon of Pushtashan assemblage trondhjemite sample N16 yielded a U-Pb age of 96.0 ± 2.0 Ma. However the oscillatory-zoned magmatic zircon displays widespread recrystallisation, accompanied with etching of the grains to give a honeycomb texture, coupled with a reduction in Th/U. Domains dominated by recrystallised zircon yielded a U-Pb age of 93.1 ± 3.5 Ma, statistically indistinguishable from the age acquired from oscillatory-zoned igneous domains. These results demonstrate that the N16 zircons were subjected to intense recrystallisation either by late magmatic hydrothermal processes or only a short time later. The zircon U-Pb results are robust evidence that the Pushtashan assemblage is Cretaceous (Cenomanian) in age and does not belong to one of the Paleogene mélange ophiolite units in the same region. The N16 zircons yielded an initial ε_{Hf} value of 13.90 ± 0.96. The error envelope of this elevated value overlaps with model depleted mantle (DM) at 96 Ma, and falls within the immediately sub-DM field for arc rocks with minimal contamination by older crust (Fig. 8).

7.2. Gabbro and norite fractional crystallisation

Major and trace element contents of Pushtashan massif show that gabbros and norites exhibit different evolutionary trends, suggesting that they followed different paths of fractional crystallization or accumulation or/and post-magmatic alteration. The presence of clinopyroxene in gabbros and the lack of clinopyroxene-orthopyroxene equilibrium in the norites indicate different origins. This observation is confirmed by more magnesian character of the norites (Mg# = 74–86) than the gabbros (Mg# = 48–63). Wide ranges of SiO_2 and Mg#, V, Cr, Co in the gabbros and norites are considered to be the result of magmatic differentiation. The major and trace elements show good linear positive and negative correlation with SiO_2, suggesting fractionation of early minerals such as olivine, pyroxenes, plagioclase and ilmenite. Thus two-stages of differentiation have been recognised; fractionation of olivine + plagioclase + clinopyroxene + Fe-Ti oxide minerals in gabbros and plagioclase + orthopyroxene + amphibole in norite. The gabbros are regarded as showing fractionation along a low-fO_2 iron-enrichment tholeiitic trend (Aditi Mandal et al., 2012). On the other hand, the norites follow a calc-alkaline trend. This is supported by positive correlations of MgO with CaO and SiO_2, and negative correlations with TiO_2, FeO^t and Al_2O_3. The positive Eu and Sr anomalies displayed by norite samples indicates most likely that cumulate plagioclase is present.

7.3. Parental melts of the Pushtashan gabbros and norites

Clinopyroxenes of the Pushtashan gabbros have moderate Mg# values of 60–75, while plagioclases have low An contents of 35. Norites have moderately high Mg# while plagioclases have moderately high An contents of 70–93. Anorthitic plagioclases are quite common in high-alumina basalts (Crawford et al., 1987) and gabbros from mid ocean ridge settings (Ross and Elthon, 1993; Dick and Natland, 1996; Ridley et al., 2006). Ca rich plagioclases are common in suprasubduction zone where H_2O fugacity is high. Low Al_2O_3 contents of the gabbro clinopyroxenes indicate that they were most likely formed through low-pressure crystallisation of magma formed by dry

Table 4
Whole rock geochemical analyses of Pushtashan igneous rocks with major (in wt.%) and supplementary trace elements (in ppm) by XRF and the REE and other trace elements by ICP-MS. See Supplementary Table 2 for additional samples with only major and supplementary trace elements by XRF.

Sample	N2	N4	N6	N7	N9	N11	N12	N27	N28	N29	AP1	N17	N19	N16	N15	N19	N21	N26
	Norite	Norite	Norite	Norite	Norite	Norite	Norite	Norite	Norite	Norite	Norite	Gabbro	Gabbro	Granodi.	Basalt	Gabbro	Basalt	Basalt
SiO_2	45.58	47.14	44.49	45.16	45.91	45.13	46.17	44.25	45.93	42.88	49.75	46.51	43.24	74.98	47.52	43.24	52.72	45.23
TiO_2	0.21	0.14	0.15	0.21	0.18	0.20	0.20	0.06	0.23	0.05	1.10	1.58	1.33	0.29	1.01	1.33	1.37	3.35
Al_2O_3	13.80	18.23	19.67	15.69	16.20	15.16	15.79	21.41	16.08	19.09	15.43	15.68	15.43	11.73	14.74	15.43	14.49	14.08
Fe_2O_3	5.64	5.79	5.55	6.77	6.59	7.52	6.99	3.79	4.53	4.94	12.42	12.65	11.44	4.28	12.39	11.44	12.21	16.27
MnO	0.10	0.12	0.09	0.12	0.11	0.10	0.12	0.06	0.08	0.07	0.19	0.19	0.17	0.06	0.21	0.17	0.12	0.18
MgO	13.50	8.64	7.02	11.10	11.95	11.24	11.14	12.12	10.63	15.67	6.36	5.94	6.13	0.63	7.65	6.13	5.73	4.50
CaO	13.29	12.94	11.94	13.64	13.37	13.18	14.23	9.01	16.24	10.78	6.23	7.95	18.37	0.50	10.67	18.37	2.14	7.13
Na_2O	1.50	2.54	2.07	1.65	1.57	1.62	1.55	1.82	1.41	1.18	4.16	3.30	0.59	5.24	2.56	0.59	5.09	4.26
K_2O	0.44	0.85	0.59	0.51	0.47	0.77	0.62	1.80	0.34	0.44	0.66	0.72	0.06	0.31	0.21	0.06	0.09	0.24
P_2O_5	0.05	0.18	0.04	0.04	0.01	0.05	0.01	0.01	0.02	0.04	0.08	0.11	0.12	0.04	0.09	0.12	0.13	0.51
LOI	4.39	4.21	6.14	3.53	3.75	2.89	4.17	6.25	4.22	6.35	2.92	3.42	2.29	1.19	2.08	2.29	4.44	3.06
Total	98.51	100.85	97.82	98.80	100.38	97.91	101.22	100.59	99.74	101.51	99.46	99.23	99.16	99.23	99.12	99.16	98.54	100.54
XRF trace elements																		
Co	56.5	34.3	39.3	57.2	51.9	43.7	54.5	59.4	46.6	62.7	40.9	39.8	50.6	8.9	42.7	50.6	37.5	36.5
Ni	292.6	40.5	35.4	173.2	227.3	161	170	486.1	215.6	596.8	33.7	35.5	54.3	13.6	44.1	54.3	12.4	19.2
Cu	104	58.1	37.7	80	95.8	117.1	119	38.6	77.1	70.7	67.0	58.5	12.3	8.9	135.2	12.3	6.7	168.9
Zn	29.2	22.8	12.9	31.1	30.7	24.2	32.6	22.1	13.3	27.3	86.5	83.6	64.7	47.5	84.8	64.7	100.9	91.6
Ga	6.5	12.1	16.4	9.3	8.2	8.2	8.2	7.4	12.9	6.8	14.9	17	22	15.8	12.7	22	14.5	21.3
Pb	<1.0	<1.0	<1.0	<1.0	<1.0	<1.0	<1.0	<1.0	<1.0	<1.0	<1.0	0.8	0.5	<1.0	<1.0	0.5	1.3	1.7
ICPMS trace elements																		
V	180	138	114	200	163	166	176	51	164	34	450	460	341	7	562	341	509	423
Cr	2190	50	50	570	620	500	490	890	1600	660	90	90	210	470	110	210	30	40
Rb	4.8	8.4	5.7	4.6	4.5	7.8	6.3	19.6	3.7	3.2	5.9	4.3	0.3	2.4	1.8	0.3	0.8	2.8
Sr	186.5	233	220	159.5	194	142	299	375	206	226	335	135.5	547	54.5	146	547	65.6	242
Y	6.2	4	5.7	7	5.4	6.4	6	2	7	1.1	27.5	29.6	27.5	58	23.6	27.5	22.3	45.8
Zr	5	3	3	15	3	4	3	2	8	2	52	70	59	226	52	59	67	298
Nb	<0.2	<0.2	0.2	<0.2	<0.2	0.2	<0.2	0.5	0.4	0.2	1	1.3	1.3	4.1	0.7	1.3	1	37.2
Cs	0.22	0.44	0.29	0.73	0.38	0.76	0.83	0.32	0.18	0.13	0.18	0.15	0.01	0.09	0.13	0.01	0.11	0.07
Ba	9	19.9	17	8.5	12.9	23.7	15.9	97	23.6	8	35.8	20.8	7.4	34.4	8.1	7.4	12.5	125
Hf	0.2	<0.2	<0.2	0.4	<0.2	0.2	0.2	<0.2	0.3	<0.2	1.6	2	1.7	6.3	1.5	1.7	2	7
Ta	<0.1	<0.1	<0.1	<0.1	<0.1	0.4	0.3	0.1	0.1	0.1	0.1	0.2	0.2	0.5	0.3	0.2	0.2	2.3
Th	<0.05	<0.05	<0.05	<0.05	<0.05	<0.05	<0.05	<0.05	0.07	<0.05	0.16	0.13	0.12	0.78	0.1	0.12	0.21	3.58
U	<0.05	<0.05	<0.05	<0.05	<0.05	<0.05	<0.05	<0.05	<0.05	<0.05	0.08	0.07	0.06	0.3	<0.05	0.06	0.25	0.93
La	<0.5	<0.5	<0.5	<0.5	<0.5	<0.5	<0.5	<0.5	0.5	<0.5	2.4	2.7	2.3	8.3	1.4	2.3	3.7	33.2
Ce	0.9	0.5	1.1	0.7	0.9	0.7	0.7	0.5	1.1	<0.5	7.4	8.1	7.5	24.4	4.9	7.5	9.8	71.5
Pr	0.15	0.09	0.18	0.15	0.14	0.15	0.15	0.08	0.22	0.05	1.24	1.37	1.3	3.75	0.87	1.3	1.57	8.76
Nd	1.1	0.5	1	1	0.8	0.9	0.8	0.4	1.2	0.2	6.4	7.3	6.7	17.9	4.8	6.7	8	35.2
Sm	0.5	0.25	0.42	0.48	0.53	0.54	0.55	0.18	0.57	0.13	2.4	2.78	2.54	6.08	2.14	2.54	2.89	8.72
Eu	0.28	0.21	0.42	0.34	0.24	0.31	0.29	0.14	0.33	0.14	0.92	1.15	1.13	1.43	0.61	1.13	1.02	3.01
Gd	0.93	0.51	0.78	0.98	0.69	0.94	0.82	0.31	0.99	0.19	3.69	4.33	3.81	7.85	3.06	3.81	3.74	9.46
Tb	0.16	0.1	0.13	0.17	0.13	0.17	0.16	0.06	0.18	0.03	0.65	0.76	0.68	1.44	0.56	0.68	0.64	1.42
Dy	1.16	0.66	0.99	1.25	0.93	1.09	1.06	0.36	1.17	0.18	4.5	5.03	4.39	9.38	3.84	4.39	4.03	8.3
Ho	0.23	0.14	0.21	0.25	0.2	0.24	0.22	0.06	0.25	0.04	0.92	1.02	0.91	1.95	0.81	0.91	0.81	1.59
Er	0.69	0.47	0.62	0.74	0.58	0.71	0.68	0.19	0.77	0.14	2.97	3.29	2.86	6.38	2.57	2.86	2.49	4.61
Tm	0.09	0.06	0.08	0.14	0.1	0.11	0.11	0.04	0.08	0.02	0.45	0.48	0.46	0.97	0.4	0.46	0.39	0.68
Yb	0.55	0.41	0.61	0.67	0.43	0.62	0.6	0.18	0.62	0.11	2.75	3.05	2.64	6.07	2.42	2.64	2.42	3.82
Lu	0.08	0.06	0.09	0.1	0.08	0.11	0.09	0.02	0.1	0.01	0.43	0.46	0.43	0.95	0.38	0.43	0.4	0.59

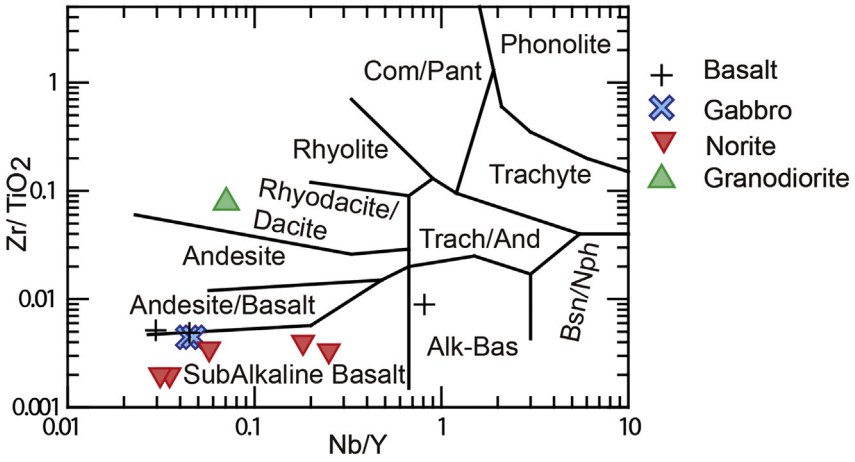

Figure 9. Nb/Y versus Zr/TiO_2 igneous discrimination plot showing general classification of Pushtashan samples.

decompressional melting of upwelling mantle in an extensional setting.

The almost flat primitive mantle-normalised rare earth element patterns of gabbros without significant Nb, Ta and Ti anomalies (Fig. 11), would support their derivation from by dry decompressional melting of asthenospheric mantle (Hofmann, 1988; Sun and McDonough, 1989). Norites show mild depletion in the light-REE with positive Eu and negative Nb, Ta and Ti anomalies, with variable enrichment in Th and Ba. This is similar to what is observed in island arc basalts (Kepezhinskas et al., 1996). Field evidence shows that the gabbros were intruded into an assemblage of basalts and andesites with interlayered sedimentary rocks plus the norites. This assemblage is thus interpreted to indicate a suprasubduction zone environment, but with the temporally later gabbros interpreted to indicate rifting of an arc.

8. Significance of the Pushtashan felsic intrusions

Granitic rocks with a genetic link to ophiolites are generated during (i) spreading, (ii) subduction or (iii) obduction of oceanic crust (Li et al., 2008). Two different types of granitic rocks are generated during seafloor spreading (Li and Li, 2003); the fractionation-type is generated by extensive fractional crystallisation of sub-alkali basaltic magmas at low pressures (Coleman and Peterman, 1975; Floyd et al., 1998; Freund et al., 2014), or the shear type by melting of amphibolite-facies metabasalts in high

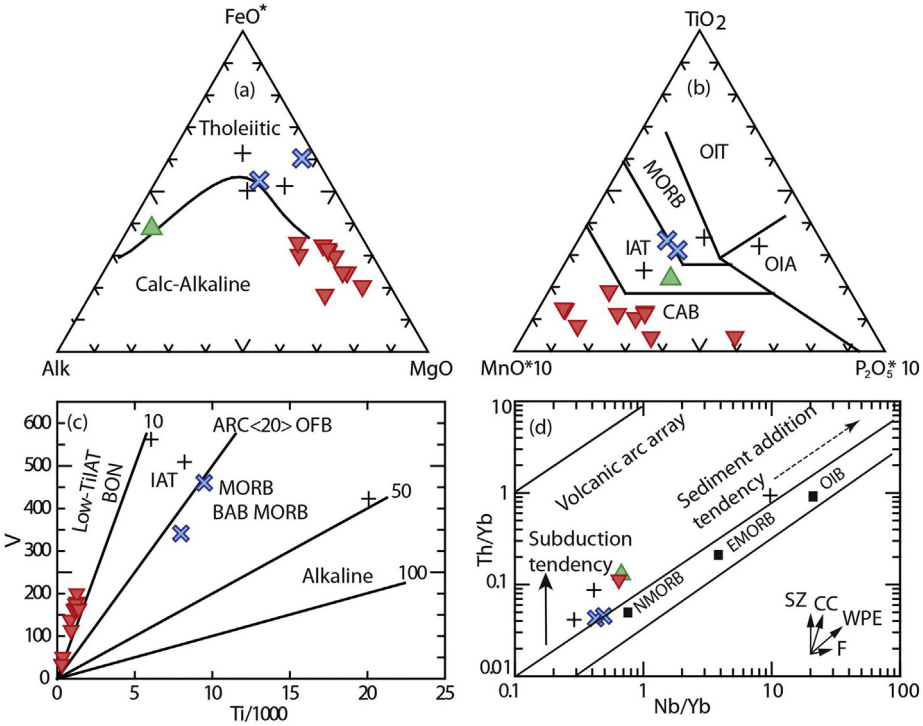

Figure 10. (a) AFM triangle (after Irvine and Baragar, 1971), showing that the norite samples fall in the calc-alkaline field, and the gabbros and basalts fall in the tholeiitic field. (b) The TiO_2-MnO-P_2O_5 diagram of Mullen (1983). (c) The Ti/1000 − V discrimination diagram of Shervais (1982). (d) Nb/Yb versus Th/Yb diagram of Pearce (2008). Symbols as for Fig. 9.

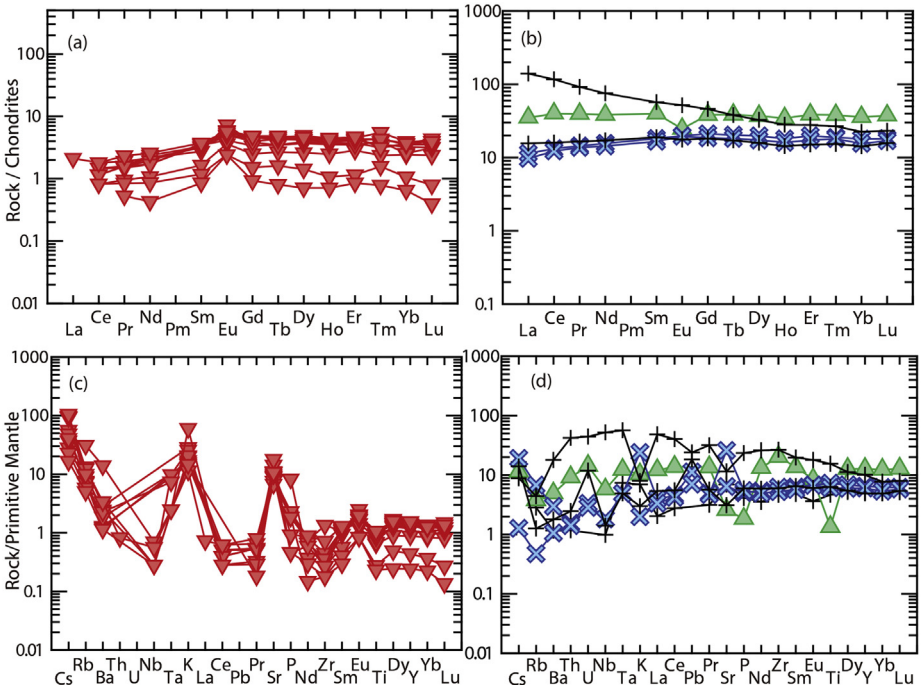

Figure 11. Chondrite-normalised REE patterns for (a) norites. (b) basalts, gabbros and trondhjemite N-16. Primitive mantle-normalised plots for (c) norites and (d) basalts, gabbros and trondhjemite N16. Symbols as for Fig. 9.

temperature shear zones in the lower parts of oceanic crust close to a spreading centre (Koepke et al., 2004, 2007). The subduction-types are produced by dehydration melting of subducted oceanic crust at high pressures with garnet and amphibole as the main residual minerals (Li and Li, 2003; Yoshikawa and Ozawa, 2007). The obduction-type originates from the melting of sedimentary rocks in marginal basins beneath ophiolite thrust sheets during the obduction of ophiolites (Pearce, 1989; Skjerlie et al., 2000; Whitehead et al., 2000).

The Pushtashan trondhjemite sample N16 displays by high Na_2O, low K_2O (<1 wt.%) and Al_2O_3 (<15 wt.%). LREE depleted pattern [$(La/Yb)_N \leq 1$] and flat trace element pattern with significant negative Sr and Ti anomalies. These are signatures observed in fractionation-type granites associated with gabbros and basaltic lavas generated during seafloor spreading (Jiang et al., 2015). The lack of depletion in the HREE indicates that genesis of these rocks did not involve partial melting at high pressure with garnet fractionation, as commonly seen in arc-related TTG suites (e.g. Martin, 1986). However, they do show similarities with arc-related TTG suites by displaying negative Nb and Ti anomalies in primitive mantle normalised spider plots (Fig. 11d). We contend that geochemical signatures could be ascribed to high heat flux in the arc during later rifting caused a low degree of low pressure partial melting in host norites and arc basalts. This could have been triggered by incursion of meteoric water in the high heat flow extensional environment which spawned the late gabbro intrusions. This would be in keeping with evidence that many ophiolites formed by spreading above subduction zones, the so-called suprasubduction zone ophiolites (Pearce et al., 1984; Shervais, 2001), which gives a complex environment for the interaction of mantle-derived gabbros with newly-formed arc crust in a high heat flow, extensional environment. Suprasubduction-style ophiolites typically formed during short-lived periods (<5 million years) of regional plate reorganisation, in narrow rifted basins where melts were contaminated by partial melting of neighbouring lower crust (Hall, 1984; Dilek et al., 1999).

8.1. Geodynamic setting of the Pushtashan assemblage in Neo-Tethys; a Cretaceous suprasubduction zone assemblage

The Iraq Zagros ophiolites (IZO) are allochthons derived from Neo-Tethys. This ocean began to form during the late Permian–early Triassic, with rifting on the north side of Gondwana (Agard et al., 2005). Evidence for the opening of Neo-Tethys is indicated by early alkaline mafic dykes and lavas within the Late Triassic rifted margins such as represented by the Hawraman platform carbonates (unpublished data).

The ophiolitic and suprasubduction zone assemblages in the IZO were emplaced in two major episodes in the late Cretaceous and Paleogene (Ismail et al., 2014). The late Cretaceous assemblages were generated when a new subduction zone was initiated on the southern flank of Eurasia (Shafaii Moghadam and Stern, 2011). Subduction initiation was accompanied by extension and incipient arcs, namely the Urumieh–Dokhtar arc in Iran and Hasanbag in Iraq.

Following the reasoning of Stern (2004), Dilek and Thy (2009) and Dilek and Furnes (2011, 2014) it is now widely recognised that most ophiolites contain geochemical signatures indicative of their formation or modification in supra-subduction zone (SSZ) environments. Most of the observed IZO ophiolites show complex variations in chemistry, with some MORB-like components, but also predominantly rocks with calc-alkaline signatures, which points to most of the IZO ophiolites representing arc-backarc and rifted arc assemblages.

As demonstrated above, the Pushtashan gabbros and norites were generated by two different processes. This multi-stage tectono-magmatic evolution of the Pushtashan ophiolite is quite similar to that of other late Cretaceous Tethyan ophiolites along the Bitlis–Zagros suture zone as well as the Oman ophiolite (Alabaster et al., 1982; Ernewein et al., 1988; Parlak et al., 2006; Dilek and Thy, 2009; Shafaii Moghadam et al., 2014). Compositional bimodality has been interpreted to have arisen from seafloor spreading during the initiation of subduction, with a lava stratigraphy from early-

erupted MORB grading upward into calc-alkaline arc boninitic lavas and/or late dykes of these affinities that crosscut the early MORB-like sequences (Stern, 2004). This geochemical progression through time is thought to be the result of various degrees of melting of highly heterogeneous and repeatedly depleted mantle source (Dilek and Thy, 2009). According to this model, all magmatic rocks (MORB, island arc tholeiites, boninites) formed in the same fore-arc region, with eruption of early MORB-like tholeiites (Reagan et al., 2010) and younger boninitic lavas (Whattam and Stern, 2011). Geochemical and geochronological data for the late Cretaceous Pushtashan assemblage indicate that most magmatic rocks have strong suprasubduction signatures.

9. Conclusions

(1) The Pushtashan assemblage is a tectonically-bounded package of basalts, andesites, gabbros, norites and serpentinite, thrust over Cenozoic red beds and itself tectonically overlain by the Cretaceous Qandil Group.
(2) The petrography, mineral chemistry and whole-rock compositions of the Pushtashan gabbros are typical of tholeiite magma crystallised under low-pressure conditions, where the norites suite is typical of calc-alkaline magma, suggesting that the source of the norites included mantle metasomatised by fluids released from subducted oceanic crust.
(3) The gabbros were intruded into volcanic rocks of both basaltic and andesitic affinity with *interlayered* sedimentary rocks. This suggests that both types of magmatism occurred in a suprasubduction zone setting.
(4) The major, trace and REE geochemistry and field relations indicate that the felsic rocks formed in the suprasubduction zone setting.
(5) The zircon U-Th-Pb-Hf isotopic data indicate that the Pushtashan assemblage is Cretaceous in age (Cenomanian) and evolved in a setting remote from continental influence. The most likely setting is an intra-oceanic arc with little or no input from continental detritus, rather than at an active margin.

Acknowledgements

This project was supported by University of Kirkuk and partially supported by the GeoQuEST Research Centre (University of Wollongong). Les Kinsley (Australian National University) is thanked for technical assistance with the zircon Lu-Hf analyses. Jose Abrantes is thanked for sample preparation for whole rock major and trace element analysis. Norman Pearson is thanked for e-probe technical support in Macquarie University.

Appendix A. Supplementary data

Supplementary data related to this article can be found at http://dx.doi.org/10.1016/j.gsf.2016.11.002.

References

Aditi Mandal, A.R., Depanath, M., Pau, S.P., 2012. Petrology, geochemistry of hornblende gabbro and associated dolerite dyke of Paharpur, Puruliya, West Bengal: implication for petrogenetic process and tectonic setting. Journal of Earth System Science 121, 793–812.
Agard, P., Omrani, J., Jolivet, L., Mouthereau, F., 2005. Convergence history across Zagros (Iran): constraints from collisional and earlier deformation. International Journal of Earth Science 94, 401–419.
Alabaster, T., Pearce, J.A., Malpas, J., 1982. The volcanic stratigraphy and petrogenesis of the Oman ophiolite complex. Contributions to Mineralogy and Petrolology 81, 168–183.
Ali, S.A., Buckman, S., Aswad, K.J., Jones, B.G., Ismail, S.A., Nutman, A.P., 2012. Recognition of Late Cretaceous Hasanbag ophiolite-arc rocks in the Kurdistan region of the Iraqi Zagros suture zone: a missing link in the paleogeography of the closing Neotethys Ocean. Lithosphere 4, 395–410.
Ali, S.A., Buckman, S., Aswad, K.J., Jones, B.G., Ismail, S.A., Nutman, A.P., 2013. The tectonic evolution of a Neo-Tethyian (Eocene–Oligocene) island-arc (Walash and Naopurdan groups) in the Kurdistan region of the Northeast Iraqi Zagros Suture Zone. The Island Arc 22, 104–125.
Ali, S.A., Mohajjel, M., Aswad, K.J., Ismail, S.A., Buckman, S., Jones, B.G., 2014. Tectono-stratigraphy and general structure of the northwestern Zagros collision zone across the Iraq-Iran border. Journal of Environment and Earth Science 4 (4), 92–110.
Ali, S.A., Ismail, S.A., Nutman, A.P., Bennett, V.C., Jones, B.G., Buckman, S., 2016. The intra-oceanic Cretaceous (~108Ma) Kata–Rash arc fragment in the Kurdistan segment of Iraqi Zagros suture zone: implications for Neotethys evolution and closure. Lithos 260, 154–163.
Arai, S., Shimizu, Y., Ismail, S.A., Ahmed, A.H., 2006. Low-*T* formation of high-Cr spinel with apparently primary chemical characteristics within podiform chromitite from Rayat, northeastern Iraq. Mineralogical Magazine 70, 499–508.
Aswad, K.J.A., Al-Samman, A.H.M., Aziz, N.R.H., Koyi, A.M.A., 2014. The geochronology and petrogenesis of Walash volcanic rocks, Mawat nappes: constraints on the evolution of the northwestern Zagros suture zone, Kurdistan Region, Iraq. Arabian Journal of Geosciences 7, 1403–1432.
Barker, F., 1979. Trondhjemite: definition, environment and hypotheses of origin. In: Barker, F. (Ed.), Trondhjemites, Dacites, and Related Rocks. Elsevier, Amsterdam, pp. 1–12.
Black, L.P., Kamo, S.L., Allen, C.M., Aleinikoff, J.M., Davis, D.W., Korsch, R.J., Foudoulis, C., 2003. TEMORA 1: a new zircon standard for Phanerozoic U-Pb geochronology. Chemical Geology 200, 155–170. http://dx.doi.org/10.1016/S0009-2541 (03)00165-7.
Bolton, C.M.G., 1956. The Geology of the Rania Area. Site. Inv. Co. Report, No. 271. GEOSURV Library, Baghdad, Iraq.
Bouvier, A., Vervoort, J.D., Patchett, J., 2008. The Lu–Hf and Sm–Nd isotopic composition of CHUR: constraints from unequilibrated chondrites and implications for the bulk composition of the terrestrial planets. Earth and Planetary Sciences Letters 273, 48–57.
Buday, T., Jassim, S.Z., 1987. Tectonism, Magmatism and Metamorphism, the Regional Geology of Iraq, Part 11. GEOSURV, Baghdad.
Coleman, R., Peterman, Z., 1975. Oceanic plagiogranite. Journal of Geophysical Research 80, 1099–1108.
Compston, W., Williams, I.S., Meyer, C., 1984. U-Pb geochronology of zircons from lunar breccia 73217 using a sensitive high mass-resolution ion microprobe. Journal of Geophysical Research 89 (Suppl.), B525–B534.
Crawford, A.J., Falloon, T.J., Eggins, S., 1987. The origin of island arc high-alumina basalts. Contributions to Mineralogy and Petrology 97, 417–430.
Dick, H.J.B., Natland, J.H., 1996. Late-stage melt evolution and transport in the shallow mantle beneath the East Pacific Rise. Proceedings of the Ocean Drilling Program, Scientific Results 147, 103–134.
Dilek, Y., Furnes, H., 2011. Ophiolite genesis and global tectonics: geochemical and tectonic fingerprinting of ancient oceanic lithosphere. Bulletin of the Geological Society of America 123, 387–411.
Dilek, Y., Furnes, H., 2014. Ophiolites and their origins. Elements 10, 93–100.
Dilek, Y., Moores, E.M., 1990. Regional tectonics of the eastern Mediterranean ophiolites. In: Malpas, J., Moores, E.M., Panayiotou, A., Xenophontos, C. (Eds.), Ophiolites, Oceanic Crustal Analogues, Proceedings of the Symposium "Troodos 1987". The Geological Survey Department, Nicosia, Cyprus, pp. 295–309.
Dilek, Y., Thy, P., 2009. Island arc tholeiite to boninitic melt evolution of the Cretaceous Kizildag (Turkey) ophiolite: model for multi-stage early arc–forearc magmatism in Tethyan subduction factories. Lithos 113, 68–87.
Dilek, Y., Thy, P., Hacker, B., Grundvig, S., 1999. Structure and petrology of Tauride ophiolites and mafic dike intrusions (Turkey): implications for the Neotethyan Ocean. Bulletin of the Geological Society of America 111, 1192–1216.
Dilek, Y., Furnes, H., Shallo, M., 2007. Suprasubduction zone ophiolite formation along the periphery of Mesozoic Gondwana. Gondwana Research 11, 453–475.
Ernewein, M., Pflumino, C., Whitechurch, H., 1988. The death of an accretion zone as evidenced by the magmatic history of the Sumail ophiolite (Oman). Tectonophysics 151, 247–274.
Floyd, P.A., Yaliniz, M.K., Goncuoglu, M.C., 1998. Geochemistry and petrogenesis of intrusive and extrusive ophiolitic plagiogranites, Central Anatolian Crystalline Complex, Turkey. Lithos 42, 225–241.
Freund, S., Haase, K., Keith, M., Beier, C., Garbe-Schönberg, D., 2014. Constraints on the formation of geochemically variable plagiogranite intrusions in the Troodos Ophiolite, Cyprus. Contributions to Mineralogy and Petrology 167, 1–22.
Hall, R., 1984. Ophiolites: fragments of ophiolitic lithosphere. In: Gass, I.G., Lippard, S.J., Shelton, A.W. (Eds.), Ophiolites and Oceanic Lithosphere, Geological Society of London Special Publication 13, pp. 393–404.
Hiess, J., Bennett, V.C., Nutman, A.P., Williams, I.S., 2009. In situ U–Pb, O and Hf isotopic compositions of zircon and olivine from Eoarchaean rocks, West Greenland: new insights to making old crust. Geochimica et Cosmochimica Acta 73, 4489–4516. http://dx.doi.org/10.1016/j.gca.2009.04.019.
Hofmann, A.W., 1988. Chemical differentiation of the earth: the relationship between mantle, continental crust and oceanic crust. Earth and Planetary Science Letters 90, 297–314.
Irvine, T.N., 1982. Terminology for layered intrusions. Journal of Petrology 23, 127–162.
Irvine, T.N., Baragar, W.R.A., 1971. A guide to the chemical classification of the common volcanic rocks. Canadian Journal of Earth Sciences 8, 523–548.

Ismail, S.A., Arai, S., Ahmed, A.H., Shimizu, Y., 2009. Chromitite and peridotite from Rayat, northeastern Iraq, as afragment of Tethyan ophiolite. Island Arc 18, 175–183.
Ismail, S.A., Tola, M.M., Paul, F.C., 2010. Platinum-group elements geochemistry in podiform chromitites and associated peridotites of the Mawat ophiolite, northeastern Iraq. Journal of Asian Earth Sciences 37, 31–41.
Ismail, S.A., Kettanah, Y.A., Chalabi, S.N., Ahmed, A.H., Arai, S., 2014. Petrogenesis and PGE distribution in the Al- and Cr-rich chromitites of the Qalander ophiolite, northeastern Iraq: implications for the tectonic environment of the Iraqi Zagros Suture Zone. Lithos 202–203, 21–36.
Iizuka, T., Komiya, T., Rino, S., Maruyama, S., Hirata, T., 2010. Detrital zircon evidence for Hf isotopic evolution of granitoid crust and continental growth. Geochimica et Cosmochimica Acta 74, 2450–2472.
Jassim, S.Z., Goff, J.C., 2006. Geology of Iraq. Brno, Czech Republic, Dolin, Prague and Moravian Museum, 341 pp.
Jiang, T., Jun Gao, J., Klemd, R., Qian, Q., Zhang, X., Xinshui Wang, X.S., Tan, Z., Zhu, Z.X., 2015. Genetically and geochronologically contrasting plagiogranites in South Central Tianshan ophiolitic mélange: implications for the breakup of Rodinia and subduction zone processes. Journal of Asian Earth Sciences 113, 266–281.
Kepezhinskas, P., Defant, M.J., Drummond, M.S., 1996. Progressive enrichment of island arc mantle by melt-peridotite interaction inferred from Kamchatka xenoliths. Geochimica et Cosmochimica Acta 60, 1217–1229.
Koepke, J., Feig, S.T., Snow, J., Freise, M., 2004. Petrogenesis of oceanic plagiogranites by partial melting of gabbros: an experimental study. Contributions to Mineralogy and Petrology 146, 414–432.
Koepke, J., Berndt, J., Feig, S.T., Holtz, F., 2007. The formation of SiO_2-rich melts within the deep oceanic crust by hydrous partial melting of gabbros. Contributions to Mineralogy and Petrology 153, 67–84.
Lagabrielle, Y., Cannat, M., 1990. Alpine Jurassic ophiolites resemble the modern central Atlantic basement. Geology 18, 319–322.
Li, W.X., Li, X.H., 2003. Adakitic granites within the NE Jiangxi ophiolites, South China: geochemical and Nd isotopic evidence. Precambrian Research 122, 29–44.
Li, W.X., Li, X.H., Li, Z.X., Lou, F.S., 2008. Obduction-type granites within the NE Jiangxi Ophiolite: implications for the final amalgamation between the Yangtze and Cathaysia Blocks. Gondwana Research 13, 288–301.
Ludwig, K.R., 2003. Isoplot 3.0: A Geochronological Toolkit for Microsoft Excel. Berkeley Geochronological Center Special Publication 4. Berkeley Geochronological Center, Berkeley, California, 70 pp.
Martin, H., 1986. Effect of steeper Archean geothermal gradient on geochemistry of subduction-zone magmas. Geology 14, 753–756.
Miyashiro, A., 1974. Volcanic rock series in island arcs and active continental margins. American Journal of Science 274, 321–355.
Mullen, E.D., 1983. $MnO/TiO_2/P_2O_5$, a minor element discriminate for basaltic rocks of oceanic environments and its implications for Petrogenesis. Earth and Planetary Science Letters 62, 53–62.
Norrish, K., Chappell, B.W., 1977. X-ray fluorescence spectrometry. In: Zussman, J. (Ed.), Physical Methods of Determinative Mineralogy, second ed. Academic Press, London, pp. 201–272.
Pandarinath, K., Dulski, P., Torres-Alvarado, I.S., Verma, S.P., 2008. Element mobility during the hydrothermal alteration of rhyolitic rocks of the Los Azufres geothermal field, Mexico. Geothermics 37, 53–72.
Parlak, O., Yilmaz, H., Boztug, D., 2006. Origin and tectonic significance of the metamorphic sole and isolated dykes of the Divrigi Ophiolite (Sivas, Turkey): evidence for slab break-off prior to ophiolite emplacement. Turkish Journal of Earth Sciences 15, 25–45.
Pearce, J.A., Lippard, S.J., Roberts, S., 1984. Characteristics and tectonic significance of supra-subduction zone ophiolites. Geological Society of London Special Publications 16, 77–94.
Pearce, J.A., 2008. Geochemical fingerprinting of oceanic basalts with applications to ophiolite classification and the search for Archean oceanic crust. Lithos 100, 14–48.
Pearce, J.A., 1989. High T/P metamorphism and granite genesis beneath ophiolite thrust sheets. Ofioliti 14, 195–211.
Polat, A., Hofmann, A.W., 2003. Alteration and geochemical patterns in the 3.7-3.8 Ga Isua greenstone belt, West Greenland. Precambrian Research 126, 197–218.
Reagan, M.K., Ishizuka, O., Stern, R.J., Kelley, K.A., O'hara, Y., Blichert-Toft, J., Bloomer, S.H., Cash, J., Fryer, P., Hanan, B.B., 2010. Fore-arc basalts and subduction initiation in the Izu-Bonin-Mariana system. Geochemistry Geophysics Geosystems 11, Q03X12.
Ridley, W.I., Perfit, M.R., Smith, M.C., Fornari, D.J., 2006. Magmatic processes in developing oceanic crust revealed in a cumulate xenolith collected at the East Pacific Rise, 9°50′N. Geochemistry, Geophysics, Geosystems 7, Q12O04.
Ross, K., Elthon, D., 1993. Cumulates from strongly depleted midocean-ridge basalt. Nature 365, 826–829.
Roulkovsky, M.F., 1961. Report on Prospecting Exploration of the Spiradeh Copper Occurrence. Manuscript report. GEOSURV, Baghdad, Iraq.
Rubatto, D., Müntener, O., Barnhoorn, A., Gregory, C., 2008. Dissolution-reprecipitation of zircon at low temperature, high pressure conditions (Lanzo Massif, Italy). American Mineralogist 93, 1519–1529.
Scherer, E., Münker, C., Mezger, K., 2001. Calibration of the lutetium–hafnium clock. Science 293, 683–687. http://dx.doi.org/10.1126/science.1061372.
Shafaii Moghadam, H., Stern, R.J., 2011. Geodynamic evolution of upper Cretaceous Zagros ophiolites: formation of oceanic lithosphere above a nascent subduction zone. Geological Magazine 148, 762–801.
Shafaii Moghadam, H., Corfu, F., Chiaradia, M., Stern, R.J., Ghorbani, G., 2014. Sabzevar Ophiolite, NE Iran: progress from embryonic oceanic lithosphere into magmatic arc constrained by new isotopic and geochemical data. Lithos 210–211, 224–241.
Shervais, J.W., 1982. Ti-V plots and the petrogenesis of modern and ophiolitic lavas. Earth and Planetary Science. Letters 59, 101–118.
Shervais, J.W., 2001. Birth, death, and resurrection: the life cycle of suprasubduction zone ophiolites. Geochemistry, Geophysics, Geosystems 2. http://dx.doi.org/10.1029/2000GC000080.
Skjerlie, K.P., Pedersen, R.B., Wennberg, O.P., De la Rosa, J., 2000. Volatile phase fluxed anatexis of metasediments during late Caledonian ophiolite obduction: evidence from the Sogneskollen Granitic Complex, West Norway. Journal of the Geological Society, London 157, 1199–1213.
Smith, A.G., 1993. Tectonic significance of the Hellenic–Dinaric ophiolites. In: Prichard, H.M., Alabaster, T., Harris, N.B.W., Neary, C.R. (Eds.), Magmatic Processes and Plate Tectonics, Geological Society of London, Special Publication 76, pp. 213–243.
Söderlund, U., Patchett, P.J., Vervoort, J.D., Isachsen, C.E., 2004. The ^{176}Lu decay constant determined by Lu–Hf and U–Pb isotope systematics of Precambrian mafic intrusions. Earth and Planetary Science Letters 219, 311–324. http://dx.doi.org/10.1016/S0012-821X(04)00012-3.
Stern, R.J., 2004. Subduction initiation: spontaneous and induced. Earth and Planetary Science Letters 226, 275–292. http://dx.doi.org/10.1016/j.epsl.2004.08.007.
Sun, S.S., McDonough, W., 1989. Chemical and isotopic systematics of oceanic basalts: implications for mantle composition and processes. Geological Society of London, Special Publications 42, 313–345.
Whattam, S.A., Stern, R.J., 2011. The 'subduction initiation rule': a key for linking ophiolites, intra-oceanic forearcs, and subduction initiation. Contributions to Mineralogy and Petrology 162, 1031–1045.
Whitehead, J., Dunning, G.R., Spray, J.G., 2000. U–Pb geochronology and origin of granitoid rocks in the Thetford Mines ophiolite, Canadian Appalachians. Geological Society of America Bulletin 112, 915–928.
Williams, S., 1998. U–Th–Pb geochronology by ion microprobe. Reviews in Economic Geology 7, 1–35.
Winchester, J.A., Floyd, P.A., 1977. Geochemical discrimination of different magma series and their differentiation products using immobile elements. Chemical Geology 20, 325–343.
Yoshikawa, M., Ozawa, K., 2007. Rb–Sr and Sm–Nd isotopic systematics of the Hayachine-Miyamori ophiolitic complex: melt generation process in the mantle wedge beneath an Ordovician island arc. Gondwana Research 11, 234–246.
Zartman, R.E., 1981. Plumbotectonics – the model. Tectonophysics 75, 135–162.